Review of Scientific Instruments

AIP Publishing

RESEARCH ARTICLE | MARCH 12 2024

Optical-pump–terahertz-probe spectroscopy in high magnetic fields with kHz single-shot detection

Blake S. Dastrup ; Peter R. Miedaner ; Zhuquan Zhang ; Keith A. Nelson

Rev. Sci. Instrum. 95, 033005 (2024)
https://doi.org/10.1063/5.0179123
CHORUS

Review of
Scientific Instruments

ARTICLE

pubs.aip.org/aip/rsi

Optical-pump–terahertz-probe spectroscopy in high magnetic fields with kHz single-shot detection

Cite as: Rev. Sci. Instrum. 95, 033005 (2024); doi: 10.1063/5.0179123
Submitted: 29 September 2023 • Accepted: 23 February 2024 •
Published Online: 12 March 2024

Blake S. Dastrup, Peter R. Miedaner, Zhuquan Zhang, and Keith A. Nelson[a)]

AFFILIATIONS

Department of Chemistry, Massachusetts Institute of Technology, Cambridge, Massachusetts 01239, USA

[a)] **Author to whom correspondence should be addressed:** kanelson@mit.edu

ABSTRACT

We demonstrate optical pump–THz probe (OPTP) spectroscopy with a variable external magnetic field (0–9 T), in which the time-dependent THz signal is measured by echelon-based single-shot detection at a repetition rate of 1 kHz. The method reduces data acquisition times by more than an order of magnitude compared to conventional electro-optic sampling using a scanning delay stage. The approach illustrates the wide applicability of the single-shot measurement approach to non-equilibrium systems that are studied through OPTP spectroscopy, especially in cases where parameters such as magnetic field strength (B) or other experimental parameters are varied. We demonstrate the capabilities of our measurement by performing cyclotron resonance experiments in bulk silicon, where we observe B-field-dependent carrier relaxation and distinct relaxation rates for different carrier types. We use a pair of economical linear array detectors to measure 500 time points on each shot, offering an equivalent performance to camera-based detection with possibilities for higher repetition rates.

INTRODUCTION

Over the past few decades, there has been growing interest in using terahertz (THz) radiation as an ultrafast probe to study charge,[1,2] lattice,[3] and spin[4–7] degrees of freedom in a wide range of materials both in and out of equilibrium.[8] In some cases, THz time-domain spectroscopy has been combined with a high external magnetic field (B-field) to enable observations of B-field-dependent excitations and phases, such as electron cyclotron resonance (CR), electron spin resonance, and emergent quantum states.[4,9–13] An ongoing experimental challenge is to integrate this approach with additional pump sources to study photoexcitation dynamics. In a typical optical-pump–THz-probe (OPTP) experiment, an optical pump pulse excites the sample into a transient non-equilibrium state, followed by a time-delayed THz probe pulse. Since the conventional THz detection method, electro-optic (EO) sampling, is also a time-resolved measurement in which the THz electric field (E-field) is probed with an optical gate pulse in an EO crystal and the relative delay is scanned in a stepwise manner, an OPTP experiment requires that at least two separate time delays be scanned to obtain a complete dataset. As a result, this approach is experimentally time-consuming, with full 2D scans often requiring a whole day or more to achieve an adequate signal-to-noise ratio (SNR). This cost of time begins to become untenable when an additional scanning parameter, such as an external B-field, is introduced into the experiment.

One route to reduced data acquisition time is to replace stepwise EO sampling with echelon-based single-shot THz detection, in which a stair-step echelon is used to create a series of temporally and spatially separated beamlets that are overlapped with the THz probe in the EO crystal and then imaged onto a camera so that each time step corresponds to a distinct set of pixels on the camera sensor.[14–16] Additionally, a recent technique relying on spectral encoding of temporal information was extended to work at high repetition rates with optical pumping.[17] However, while these methods have been successfully implemented and used for time-domain THz spectroscopy,[18–20] including in pulsed magnetic fields,[16] previous implementations have not enabled shot-to-shot balancing at kilohertz repetition rates due to the difficulty of retrieving THz signals at a high speed using classical balanced detection.[15,16] One modification to the existing single-shot paradigm that was recently employed for two-dimensional THz spectroscopy uses a cylindrical lens to focus the two orthogonal polarizations of the gate beam onto a small region of the camera sensor to allow kHz readout.[14] Here, we report the adaptation of this approach for the more widely conducted optical-pump–THz-probe (OPTP) measurement, using a pair of economical 1D array detectors to perform shot-to-shot balanced detection in place of the specialized and expensive high-speed camera used previously. To test the capabilities of our setup, we measured the spectro-temporal evolution and B-field dependence of electron CR in bulk high-resistivity Si following an 800 nm optical excitation pulse. The results illustrate the versatile applicability of the method to a wide range of OPTP measurements, in which optical pumping gives rise to electronic, vibrational, or spin evolution that can be probed by THz spectroscopy.

EXPERIMENTAL

A schematic illustration of our high B-field single-shot OPTP setup is shown in Fig. 1. The setup consists of two high energy pump beam paths and one low energy gate beam path, all derived from the 4 mJ, 100 fs output of a Ti:sapphire regenerative amplifier (Coherent Astrella F-1K) with an 800 nm center wavelength. The gate beam used for single-shot readout of the THz signal is split from the main beam with a 90:10 beam splitter. The remaining portion of the main beam is split using a 60:40 beam splitter into the two pump beams with energies of roughly 2 and 1.6 mJ used for THz generation and optical pumping, respectively. The THz generation beam is directed onto a 1 mm thick zinc telluride (ZnTe) crystal with a 10 mm diameter (Ø) clear aperture (Eksma optics), which is completely filled by the 11 mm spot size of the THz generation beam. A slowly diverging THz beam (Rayleigh range ~0.25 m at 1 THz) emerges from the crystal and propagates into the Ø 100 mm bore of a superconducting solenoid magnet (0–9 T) parallel to the applied magnetic field, $\boldsymbol{B}_{\text{ext}}$. A four-rod aluminum cage structure extends through the magnet bore (500 mm length) and is mounted to the optical table at both ends of the magnet. A pair of 1 inch paraboloid mirrors (90°, EFL = 1 in.) are fixed to an optical mount, which is mounted to the four cage rods and positioned at the B-field center [see Fig. 1(b)]. The THz beam is focused onto the sample with a beam diameter of ~1 mm by one of the paraboloids, and the transmitted THz signal is collected by the other and directed out of the bore parallel to $\boldsymbol{B}_{\text{ext}}$. Outside the magnet bore, the THz beam is collected by a 2 in. paraboloid mirror (15°, EFL = 20 in.) and then focused by using a second 2 inch paraboloid mirror (90°, EFL = 4 in.) onto a 2 mm thick ZnTe crystal for EO detection. The 1.6 mJ beam used for optical pumping is delayed with an optical delay line and then demagnified with a 3:1 telescope (L1′:L2′) to a spot size of ~3 mm. A periscope is used to displace the optical pump beam vertically with respect to the THz generation beam, after which the beam is directed onto the magnet bore parallel to the THz generation beam. In the bore, a Ø 0.5 in. silver mirror mounted to the cage mount above the focusing paraboloid reflects the optical pump onto the sample at a polar angle of ~46° with respect to the sample normal.

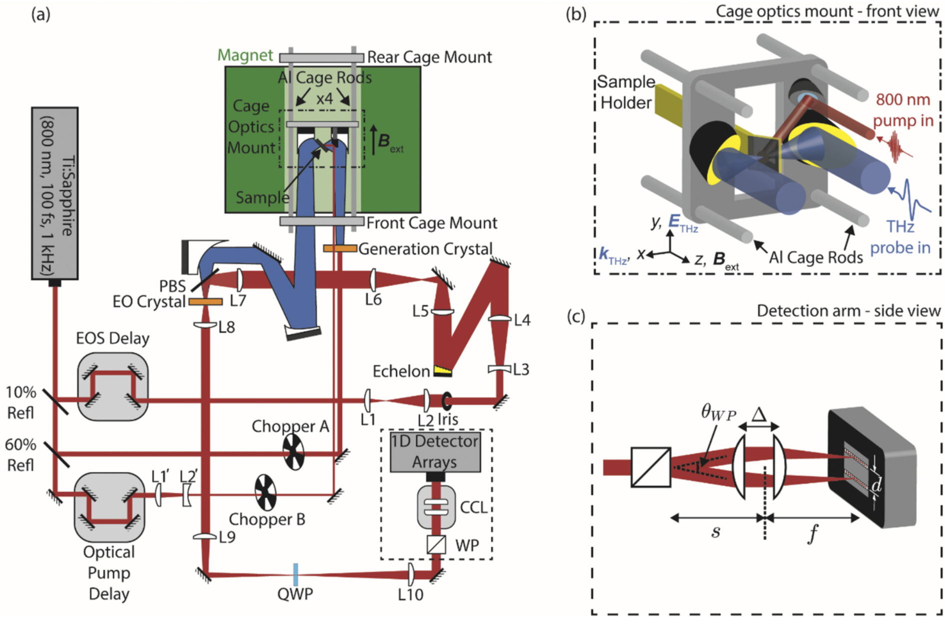

FIG. 1. Single-shot high B-field OPTP optical setup. (a) Schematic of the experimental setup. $\boldsymbol{B}_{\text{ext}}$: external B-field; BS: beam splitter; $\boldsymbol{k}_{\text{THz}}$: THz propagation direction; $\boldsymbol{E}_{\text{THz}}$: THz E-field polarization direction; HWP: half waveplate; QWP: quarter waveplate; WP: Wollaston prism; CCL: compound cylindrical lens; L1-L4, probe beam expanding telescopes (1:3); L5-10, three successive 4f imaging systems (f = 10, 10, 10, 5, 30, 30 cm); L1′ (f = 20 cm); L2′ (f = −7.5 cm); and PBS: pellicle beam splitter. (b) Front view of the in-bore cage optics mount. The THz beam path is shown in blue. The optical pump path is shown in red. The sample mount with the 45° tilt is depicted in gold. (c) Side view of the probe beam path through the Wollaston prism and compound cylindrical lens, which focuses the two probe arms onto the two 1D array detectors.

The EO sampling gate beam is delayed using an optical delay line and then expanded by a total of 9x with two separate 1:3 telescopes (L1:L2 and L3:L4) to create a roughly uniform intensity profile that fills the echelon. The stair-step echelon (Sodick) is a silver-coated reflective optic with 500 steps of 60 μm width and 7 μm height. The enlarged beam is reflected from the echelon, creating a sequence of 500 pulses with an interpulse delay of ~40 fs, which corresponds to an overall time window of ~20 ps. The beam at the echelon plane is relayed to an image plane intermediate between the echelon and the detection crystal using a 4f imaging system (L5:L6). The image is then focused by L7 and recombined with the THz beam using a pellicle beam splitter (PBS) so the two beams are focused together on the EO detection crystal. After the crystal, the optical beam is recollimated by using lens L8, which forms the end of the second 4f imaging system (L7:L8). A third 4f imaging system (L9:L10) relays the image after L8 to the detection plane. A quarter waveplate is inserted into the beam path, which serves to balance the intensity of the gate beam into any set of orthogonal polarizations, and a 10° Wollaston prism, which separates the gate beam into two orthogonal polarizations. The two polarization components are parallelized and focused by using a compound cylindrical lens [a pair of two separated cylindrical lenses, as shown in Fig. 1(c)] set to achieve both focusing and optimal spacing (see the supplementary material) onto a pair of parallel 1D detector arrays (Synertronic Glaz LineScan-I-Gen2) with 12 mm spacing, which are read out at a frame rate of 1 kHz to achieve shot-to-shot balancing.

We employ a differential chopping data collection scheme using two choppers that are inserted into the two pump beam paths and triggered using the 1 kHz trigger obtained from the laser. Labeling the THz generation beam "A" and the optical pump "B," chopper A runs at 500 Hz blocking every other pulse, while chopper B runs at 250 Hz blocking every other set of two pulses. Together, the two choppers produce each of the four combinations $\mathrm{A_{on}/B_{on}}$, $\mathrm{A_{on}/B_{off}}$, $\mathrm{A_{off}/B_{on}}$, and $\mathrm{A_{off}/B_{off}}$ over the course of four consecutive laser shots. We can thereby obtain the THz probe waveform (A), optical pump reference (B), the THz-probe waveform with optical pumping (AB), and the differential signal as follows:

$$\frac{\Delta I_\alpha}{I} = \frac{I_\alpha^+}{2I_0^+} - \frac{I_\alpha^-}{2I_0^-} = \frac{I_\alpha^+ - I_\alpha^-}{I_0}, \tag{1}$$

$$\frac{\Delta I_{\mathrm{diff}}}{I} = \frac{\Delta I_{\mathrm{AB}}}{I} - \frac{\Delta I_{\mathrm{A}}}{I} - \frac{\Delta I_{\mathrm{B}}}{I}, \tag{2}$$

where I_α^+ and I_α^- are the raw 1D gate arrays for the two polarization arms of the balanced detection scheme ($\alpha = \{A, B, AB\}$) and I_0^+ and I_0^- are the reference 1D gate arrays obtained when both the pump beams are blocked by their respective choppers. The final equality in Eq. (1) is true only when $I_0^+ = I_0^- = I_0/2$, which implies perfect balancing. We observe slight deviations (no larger than ~5%) in balancing from pixel to pixel, which we estimate leads to uncertainties in THz field amplitudes of ~0.5% (details presented in the supplementary material).

The THz transmission measurements were performed in the Voigt geometry ($\boldsymbol{k}_{\mathrm{THz}} \perp \boldsymbol{B}_{\mathrm{ext}}$). A [100] undoped high-resistivity Si sample with a thickness of 0.5 mm was mounted in a liquid helium cryostat with c-cut sapphire windows and a 1 in. path length from window to window. The cryostat was fixed to the mounting plate of a 600 mm linear stage and inserted into the gap between the two 1 in. paraboloid mirrors through a rectangular opening in the mount. For the THz transmission experiments, the sample was oriented with the [100] axis either at 90° or 45° with respect to $\boldsymbol{B}_{\mathrm{ext}}$ (where the angle is a rotation in the [011] plane of the sample). The measurements in the 90° orientation were made by mounting the sample to a copper sample mount with a Ø 2 mm aperture, while measurements in the 45° orientation were made by mounting the sample to an angled copper sample mount with Ø 3 mm clear aperture. In both the cases, the sample was cooled to a temperature of 5 K. The 800 nm optical pump was set to a pulse energy of ~7 μJ, with corresponding fluences of 70 μJ/cm^2 for the 90° orientation and 50 μJ/cm^2 for the 45° orientation. Using higher pump fluence led to the loss of CR signal.

RESULTS AND DISCUSSION

To test the performance of our single-shot detection setup, we compare the THz waveform and spectrum measured by single-shot detection to that measured by conventional detection [see Figs. 2(a) and 2(b)]. The THz signal was measured in the absence of a sample by both the methods using the same optical setup (for conventional detection, two additional mirrors were inserted into the gate beam path to bypass the echelon, and photodiodes were used in place of the 1D detector arrays). Figure 2(c) shows the raw 1D arrays obtained from each 1D array averaged over 1000 shots. The THz waveform shown in Fig. 2(b) was extracted from the raw signal by calculating $\Delta I_\alpha/I$, as given in Eq. (1), on a shot-to-shot basis and averaging over 10 000 shots (single-shot) or 500 shots per time point (conventional). For single-shot detection, this extraction yields the THz waveform as a function of the pixel number. We then used the calibration procedure described by Gao *et al.*[14] to correlate pixel number with the real-time axis as well as to correct for amplitude non-uniformity.

A comparison of the noise levels obtained by single-shot detection vs conventional detection was made by plotting the noise level of a 20 ps time window against the number of total laser shots collected for a given measurement [see Fig. 2(d)]. The gate delay line was positioned to detect a featureless time window before the arrival of the THz pulse. Each single-shot measurement captures a 20 ps time window and contains 500 time points, so a conventional scan with an equivalent step width requires 500× the number of laser shots to achieve the same time window. We performed two sets of conventional scans with 6 μm (40 fs) step width and 20 μm (133 fs) step width, the latter to allow for a more direct comparison of noise levels for measurements that do not require the spectral bandwidth (~10 THz) afforded by the short time step. Our measurements show more than an order of magnitude lower noise level for single-shot detection over conventional detection for an equal number of shots, which is consistent with the previous report utilizing a high-speed camera as the detector.[14] To explain the expected increase in SNR, it should be noted that in a standard electro-optic sampling system, the SNR does not depend on the absolute intensity of the gate beam so long as the intensity is beyond the noise floor of other elements in the system, such as the detector and ambient lab conditions, which is typically achieved. Thus, a single-shot detection scheme in theory does not suffer from a decrease in intensity when separating the pulse into beamlets, and the increase in performance is obtained from full parallel detection of all time points and the lack

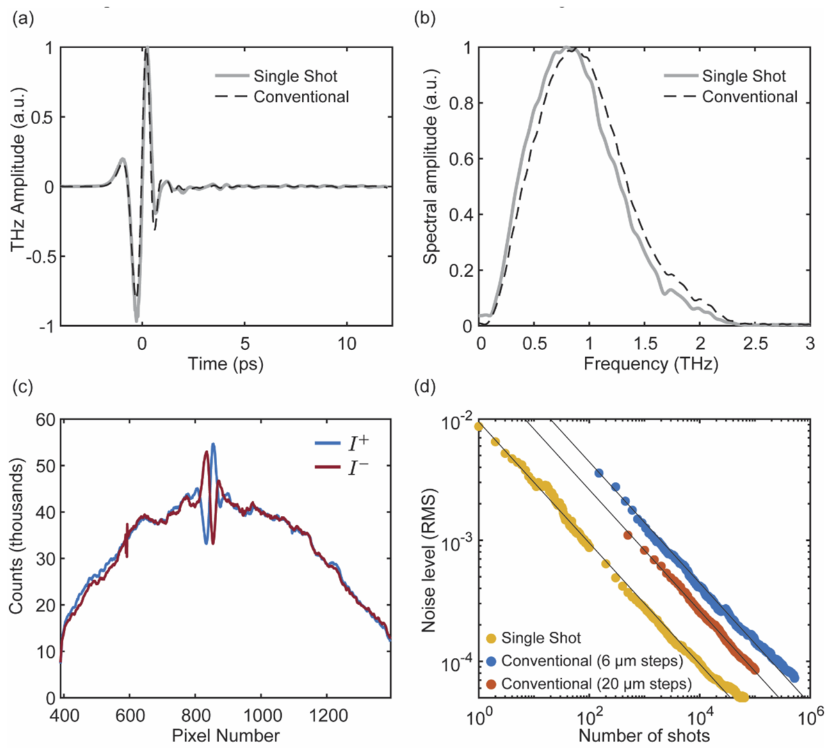

FIG. 2. Characterization of single-shot detection performance. (a) Time-domain and (b) frequency-domain comparison of the THz waveform collected with single-shot detection (solid gray line) and conventional stepwise detection with 6 μm steps (dotted black curve). (c) Raw probe signal on 1D detector arrays with the THz signal present. The plus and minus polarizations are normalized by the probe reference (without THz signal) and then subtracted from each other on a shot-to-shot basis. (d) Noise level analysis comparing the RMS noise level in a featureless region of the time-domain signal for single shot (yellow), conventional detection with 20 μm time steps (red), and conventional detection with 6 μm time steps (blue).

of an optical delay stage, drastically reducing data acquisition times. If the detected signal change is extremely weak, approaching the shot noise limit, the SNR will be constrained by the intrinsic readout noise. This limitation does not apply to the present study or to a wide range of practical applications. In practice, multi-element detectors are inherently noisier, and pointing fluctuations can be more significant on smaller pixel sizes, leading to less than perfect SNR increases. Beyond this, conventional detection also suffers from laser fluctuations, which will add noise from one time point to another since they are acquired with multiple shots. In a single-shot detection scheme, all time points are collected with the same pulse, and thus, any laser fluctuations only lead to changes in the overall strength of the entire time-dependent signal.

To showcase the measurement capabilities of our setup, we have measured electron CR in bulk undoped Si following optical excitation at 800 nm in an external B-field , which was swept from 0 to 9 T. THz-frequency CR in bulk undoped Si has previously been reported for a single-shot THz measurement in a pulsed magnetic field at a low repetition rate.[16] Those measurements were conducted with a fixed (100 ps) delay between the optical pump and THz probe pulses. Time-resolved carrier dynamics have been measured in other systems by techniques such as optical reflectivity[21] and far-IR transmission spectroscopy.[22,23] Our measurement scheme allows for the collection of the full spectral content of the THz probe with the delay τ between the optical pump and the THz probe varying over a 600 ps range and the external B-field varying from 0 to 9 T, which provides additional spectral information that allows the dynamics of different carrier types to be observed independently. Raw time-domain plots and time traces at selected optical-pump–THz-probe time delays are shown in Fig. 3. The acquisition time of the complete B-field sweep (0–9 T) was 10.3 hrs. We estimate that the present study would have required more than 11 days of data acquisition with conventional THz detection. The dependence of CR signals on the sampling delay time t is discussed briefly in the Supplementary Information, Sec. S9. Figure 4 shows plots of the THz absorption spectrum as a function of optical-pump–THz-probe delay at different B-fields. The absorption spectrum, $A(\Omega)$, was calculated as

$$A(\Omega) = -\log\left(\frac{\Delta I_{AB}/I}{\Delta I_A/I}\right), \tag{3}$$

which is valid in the linear response regime. The plots show a zero-frequency Drude response at 0 T, which decays within ~200 ps. As the B-field is increased, this zero-frequency response resolves into a set of four absorption peaks that undergo a blue shift with an increasing B-field. These four resonances can be attributed to two electron and two hole carrier types with distinct effective masses

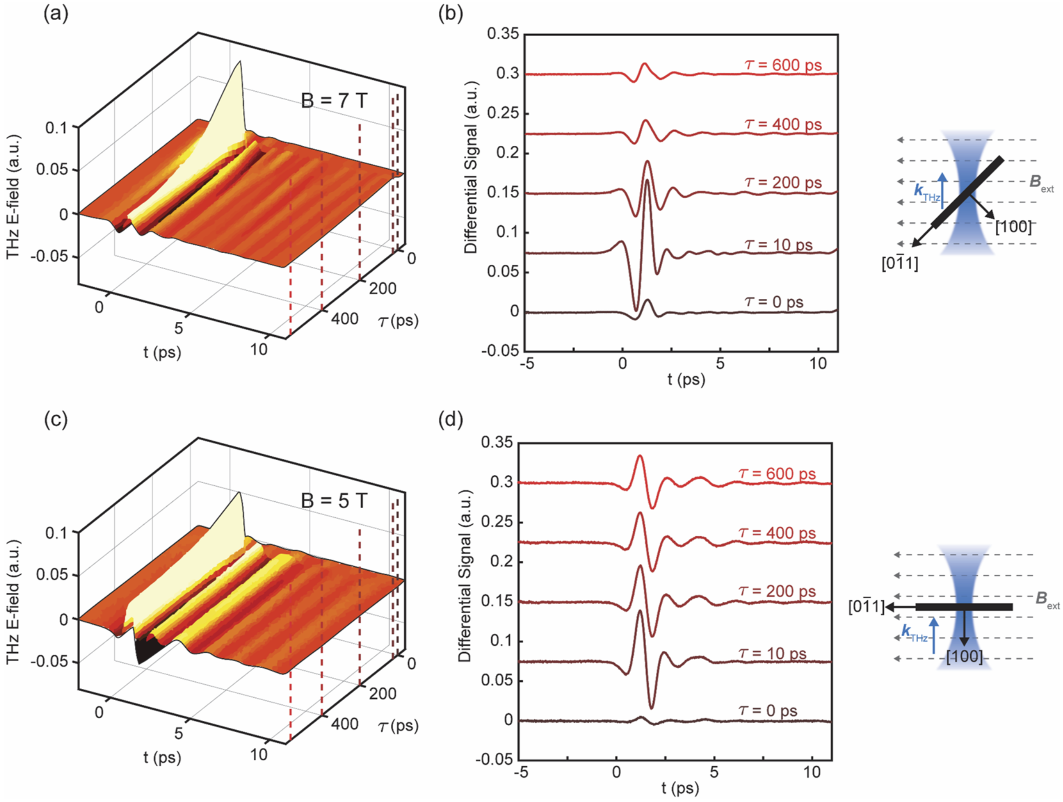

FIG. 3. Representative cyclotron resonance time-domain data from [100] high-resistivity silicon. Data were collected with $\boldsymbol{E}_{\mathrm{THz}} \perp \boldsymbol{B}_{\mathrm{ext}}$ and $\boldsymbol{k}_{\mathrm{THz}} \perp \boldsymbol{B}_{\mathrm{ext}}$ (Voigt geometry). 2D time–time plots are shown for sample orientations of (a) 45° and (c) 90° with respect to $\boldsymbol{B}_{\mathrm{ext}}$ at B = 7 T and B = 5 T, respectively, with optical-pump–THz-probe time delays $\tau = \{0,\ 10,\ 200,\ 400,\ 600\}$ ps. Constant τ -slices are plotted for the same sample configurations and B-fields in (b) and (d). The measurement configuration for each set of plots is shown by the diagram on the right.

that have been observed in previous CR experiments in bulk Si.[24] Charge carriers are generated when absorption of the 800 nm pump promotes electrons into any of the six equivalent conduction band valleys near the X point at the zone boundary, leaving holes in the two valence bands at the Si Γ-point. Under the parabolic band approximation, the constant energy surfaces of the valence band maxima are spheroidal, and those of the conduction band valleys are ellipsoidal.[24] These ellipsoids have principal axes oriented along the crystalline axes such that when the sample is rotated, the curvature of the path traversed by the electron in k-space is altered, leading to the observation of an orientation-dependent effective mass.[24,25] Because the applied B-field is oriented in the [011] plane of the sample, the CR frequencies from conduction band electrons in the four valleys in the [100] plane will be equivalent, as well as the frequencies of electrons in the two valleys parallel to the [100] axis (in the [011] plane). Thus, we refer to electron resonances as [100] electrons from the four valleys in the [100] plane, and [011] electrons from the two remaining valleys in the [011] plane. We refer to the two hole resonances as light and heavy holes. From the absorption spectra, we extracted the frequency of each resonance via simultaneous fitting to four Lorentzian functions. In Figs. 4(b) and 4(d), we have plotted the center frequencies of the four resonances obtained from these fits as a function of the applied B-field. We have excluded points at low B-field, in which the resonances are not sufficiently resolved to give good fits, as well as points at $B = 8, 9$ T for the light hole in the 45° sample orientation where the resonance is near the edge of the THz bandwidth and a good quality Lorentzian fit could not be obtained. In the 45° sample orientation, the [100] and [011] electron CR frequencies are nearly degenerate, such that the peaks in the THz absorption spectrum corresponding to these resonances have a high degree of overlap at the low B-field. The frequency of the light hole lies just above those of the two electrons and the heavy hole just below. The corresponding effective masses for these resonances in order of increasing mass are $m^* = \{0.19 \pm 0.003, 0.26 \pm 0.003, 0.30 \pm 0.005, 0.50 \pm 0.02\}m_e$, which are in good agreement within our experimental uncertainty with values reported by Dresselhaus *et al.*[24] (m_e is the free electron mass). For the 90° sample orientation, we observe the corresponding effective masses $m^* = \{0.19 \pm 0.02, 0.244 \pm 0.002, 0.42 \pm 0.03, 0.64 \pm 0.03\}m_e$, which agree within uncertainties with the literature values, but note that the heavy hole mass deviates from the expected trend in which the mass decreases going from 45° to 90° (as shown in Fig. S7).

By measuring the entire 2D dataset, we get complete spectral and temporal information about the photoinduced THz absorption,

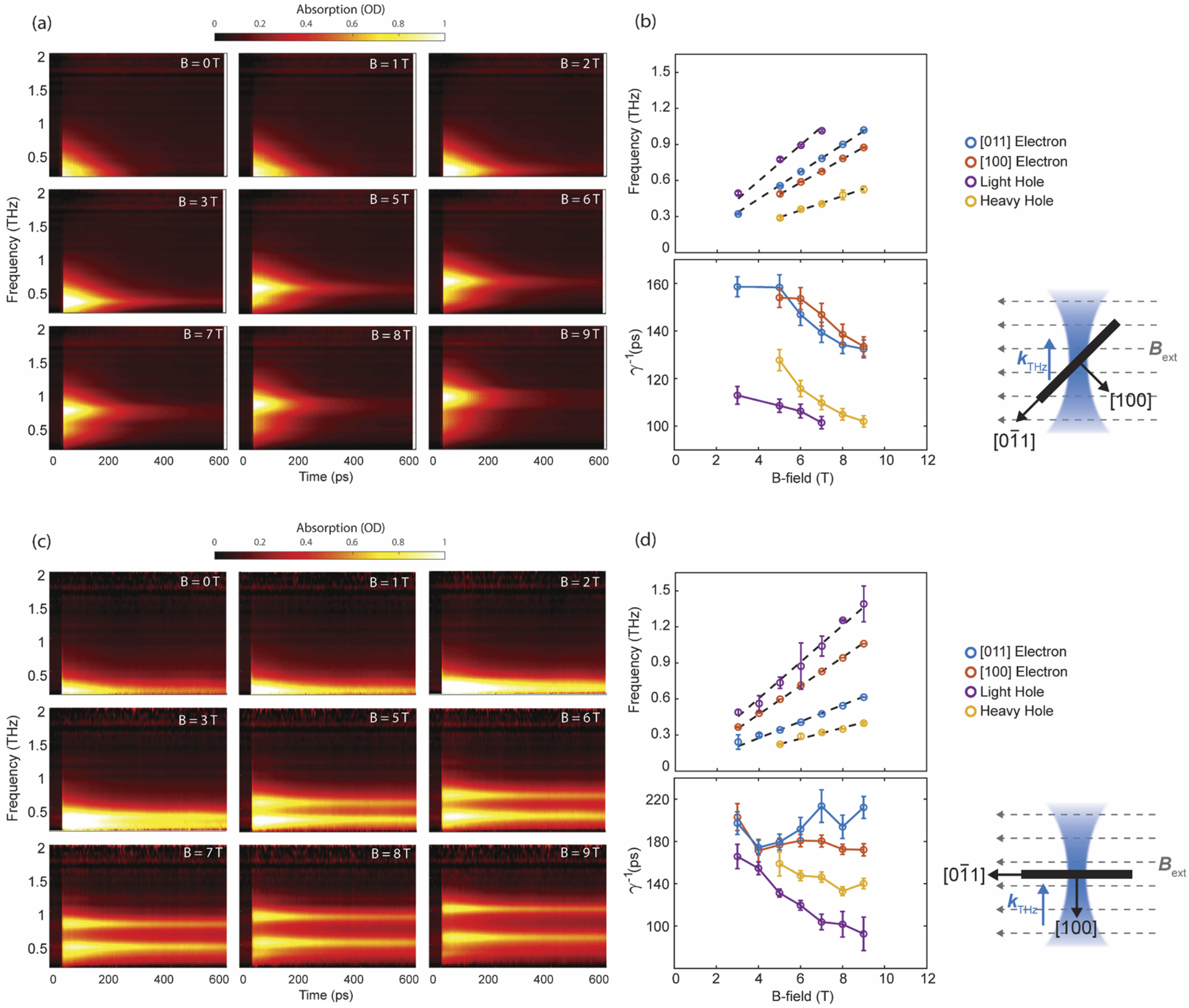

FIG. 4. Cyclotron resonance spectra from [100] high-resistivity silicon. THz absorption as a function of optical pump/THz time delay plotted for $|\boldsymbol{B}_{\text{ext}}| = 0$–9 T and samples oriented at (a) 45° and (c) 90° with respect to $\boldsymbol{B}_{\text{ext}}$ as depicted by the diagrams on the right hand side of the figure. (b) and (d) CR center frequencies (top) and inverse decay constant (bottom) as a function of external B-field. Error bars are the 95% confidence intervals extracted from (top) Lorentzian fits of the resonances and (bottom) exponential fits of the decay curves. The relationship between CR frequency and carrier effective mass is given by $\omega_c = eB/m^*$, where e is the electron charge and m^* is the effective mass. We see four distinct resonances at both 45° and 90° sample orientations. Carrier relaxation is resolved into the four carrier types, and we see distinct decay times for each carrier as well as a general trend of decreasing carrier lifetime with an increasing B-field, with some exceptions.

allowing us to extract decay dynamics individually for each carrier type, as shown in Figs. 4(b) and 4(d). To obtain these plots, decay curves for each of the four resonances were fit to an exponential function of the form, $f(\tau) = \exp(-\gamma\tau)$, where γ is the decay rate constant. The decay dynamics are drastically shorter than those observed in previous OPTP studies of silicon at room temperature,[17] which has been previously explained by Suzuki and Shimano as the slow formation of excitons at cryogenic temperatures.[26] Additionally, we observe that the electrons decay more slowly than the holes for both the 45° and 90° sample orientations. We also observe that all four of the carrier types exhibit B-field-dependent decay times. For the 45° sample orientation, the decay time constant for all four resonances decreases nearly monotonically with an increasing B-field. For the 90° sample orientation, we also see clear differences among decay time constants for the different carrier types as well as B-field dependence. In this case, the decay time of the hole resonances decreases with an increasing B-field, while that of the [011] electron is relatively flat, and the decay time of the [100] electron appears to increase with an increasing B-field. B-field dependence of carrier relaxation has previously been observed in graphene,[21,27] where it was argued that the nonuniform spacing of Landau levels in the presence of a B-field gave rise to a decrease in Auger scattering events and thereby an increased carrier lifetime. Here, we generally observe the opposite trend (relaxation rate increases with an increasing B-field). However, Landau level splitting in bulk Si is essentially harmonic, giving rise to states that are symmetrically distributed about the carrier energy. Furthermore, Landau level degeneracy increases with an increasing B-field,[28] which leads to an increased density of states in the vicinity of the carrier energy. These two effects together make it likely that the changes in level spacing and degeneracy alter the available scattering pathways as the magnetic field increases, which, in turn, leads to an observable increase in the decay rate of excited carriers.

CONCLUSION

We have constructed a variable B-field optical-pump–THz-probe spectroscopy setup with single-shot detection that allows for shot-to-shot balancing at a repetition rate of 1 kHz with the use of 1D linear array detectors. We observe SNR on par with what has recently been demonstrated for single-shot 2D THz spectroscopy based on a high-speed camera. This setup allows for the collection of full 2D optical-pump–THz-probe scans at different magnetic fields, effectively a 3D measurement, in a dramatically reduced amount of time compared to conventional EO sampling of the THz probe. The present cyclotron resonance measurements of photoexcited carriers in silicon have yielded magnetic field-dependent electron and hole effective masses and decay rates that are distinct among the different carrier types. The capabilities demonstrated in this measurement have the potential to enable new dynamical studies of low-energy magnetic excitations and other phenomena in a wide range of materials. The single-shot measurement approach will facilitate systematic optical-pump–THz-probe studies with any of a wide variety of variables, including optical and/or THz pulse fluence or polarization, applied electric field or pressure, and others.

SUPPLEMENTARY MATERIAL

Full time-domain data, details regarding automated alignment procedures, data fitting, and theoretical discussion on the cyclotron transitions can be found in the supplementary material.

ACKNOWLEDGMENTS

This work was supported by the U.S. Department of Energy, Office of Basic Energy Sciences, under Award No. DE- SC0019126.

AUTHOR DECLARATIONS

Conflict of Interest

The authors have no conflicts to disclose.

Author Contributions

B.S.D. and P.R.M. contributed equally to this work.

Blake S. Dastrup: Conceptualization (equal); Formal analysis (equal); Methodology (equal); Writing – original draft (equal); Writing – review & editing (equal). **Peter R. Miedaner**: Conceptualization (equal); Formal analysis (equal); Methodology (equal); Writing – original draft (equal); Writing – review & editing (equal). **Zhuquan Zhang**: Conceptualization (equal); Formal analysis (equal); Writing – review & editing (equal). **Keith A. Nelson**: Conceptualization (equal); Resources (equal); Supervision (equal).

DATA AVAILABILITY

The data that support the findings of this study are available from the corresponding author upon reasonable request.

REFERENCES

[1] R. Ulbricht, E. Hendry, J. Shan, T. F. Heinz, and M. Bonn, “Erratum: Carrier dynamics in semiconductors studied with time-resolved terahertz spectroscopy [Rev. Mod. Phys. 83, 543 (2011)],” Rev. Mod. Phys. **89**, 029901 (2017).

[2] Y. Lan, X. Tao, X. Kong, Y. He, X. Zheng, M. Sutton, M. G. Kanatzidis, H. Guo, and D. G. Cooke, “Coherent charge-phonon correlations and exciton dynamics in orthorhombic $CH_3NH_3PbI_3$ measured by ultrafast multi-THz spectroscopy,” J. Chem. Phys. **151**, 214201 (2019).

[3] M. Porer, U. Leierseder, J.-M. Menard, H. Dachraoui, L. Mouchliadis, I. E. Perakis, U. Heinzmann, J. Demsar, K. Rossnagel, and R. Huber, “Non-thermal separation of electronic and structural orders in a persisting charge density wave,” Nat. Mater. **13**, 857–861 (2014).

[4] X. Li, M. Bamba, N. Yuan, Q. Zhang, Y. Zhao, M. Xiang, K. Xu, Z. Jin, W. Ren, G. Ma *et al.*, “Observation of Dicke cooperativity in magnetic interactions,” Science **361**, 794–797 (2018).

[5] T. Makihara, K. Hayashida, G. T. Noe II, X. Li, N. Marquez Peraca, X. Ma, Z. Jin, W. Ren, G. Ma, I. Katayama *et al.*, “Ultrastrong magnon–magnon coupling dominated by antiresonant interactions,” Nat. Commun. **12**, 3115 (2021).

[6] Z. Z. Zhang, F. Y. Gao, J. B. Curtis, Z.-J. Liu, Y.-C. Chien, A. von Hoegen, M. T. Wong, T. Kurihara, T. Suemoto, P. Narang, E. Baldini, and K. A. Nelson, “Terahertz field-induced nonlinear coupling of two magnon modes in an antiferromagnet,” Nat. Phys. **12**, 4837 (2024).

[7] Z. Z. Zhang, F. Y. Gao, Y.-C. Chien, Z.-J. Liu, J. B. Curtis, E. R. Sung, X. Ma, W. Ren, S. Cao, P. Narang, A. von Hoegen, E. Baldini, and K. A. Nelson, “Terahertz-field-driven magnon upconversion in an antiferromagnet,” Nat. Phys. **12**, 4837 (2024).

[8] C. A. Belvin, E. Baldini, I. O. Ozel, D. Mao, H. C. Po, C. J. Allington, S. Son, B. H. Kim, J. Kim, I. Hwang *et al.*, “Exciton-driven antiferromagnetic metal in a correlated van der Waals insulator,” Nat. Commun. **12**, 4837 (2021).

[9] X. Wang, D. J. Hilton, L. Ren, D. M. Mittleman, J. Kono, and J. L. Reno, “Terahertz time-domain magnetospectroscopy of a high-mobility two-dimensional electron gas,” Opt. Lett. **32**, 1845–1847 (2007).

[10] J. Lu, I. O. Ozel, C. A. Belvin, X. Li, G. Skorupskii, L. Sun, B. K. Ofori-Okai, M. Dinca, N. Gedik, and K. A. Nelson, “Rapid and precise determination of zero-field splittings by terahertz time-domain electron paramagnetic resonance spectroscopy,” Chem. Sci. **8**, 7312–7323 (2017).

[11] A. Baydin, T. Makihara, N. M. Peraca, and J. Kono, “Time-domain terahertz spectroscopy in high magnetic fields,” Front. Optoelectron. **14**, 110–129 (2021).

[12] D. J. Hilton, T. Arikawa, and J. Kono, “Cyclotron resonance,” Charact. Mater. **2**, 1–15 (2012).

[13] C. M. Morris, N. Desai, J. Viirok, D. Hüvonen, U. Nagel, T. Rõõm, J. W. Krizan, R. J. Cava, T. M. McQueen, S. M. Koohpayeh *et al.*, “Duality and domain wall dynamics in a twisted Kitaev chain,” Nat. Phys. **17**, 832–836 (2021).

[14] F. Y. Gao, Z. Zhang, Z.-J. Liu, and K. A. Nelson, “High-speed two-dimensional terahertz spectroscopy with echelon-based shot-to-shot balanced detection,” Opt. Lett. **47**, 3479–3482 (2022).

[15] G. Mead, I. Katayama, J. Takeda, and G. A. Blake, “An echelon-based single shot optical and terahertz Kerr effect spectrometer,” Rev. Sci. Instrum. **90**, 053107 (2019).

[16] G. T. Noe, I. Katayama, F. Katsutani, J. Allred, J. A. Horowitz, D. M. Sullivan, Q. Zhang, F. Sekiguchi, G. L. Woods, M. C. Hoffmann *et al.*, "Single-shot terahertz time-domain spectroscopy in pulsed high magnetic fields," Opt. Express **24**, 30328–30337 (2016).

[17] N. Couture, W. Cui, M. Lippl, R. Ostic, D. J. J. Fandio, E. K. Yalavarthi, A. Vishnuradhan, A. Gamouras, N. Y. Joly, and J.-M. Menard, "Single-pulse terahertz spectroscopy monitoring sub-millisecond time dynamics at a rate of 50 kHz," Nat. Commun. **14**, 2595 (2023).

[18] B. K. Ofori-Okai, A. Descamps, J. Lu, L. E. Seipp, A. Weinmann, S. H. Glenzer, and Z. Chen, "Toward quasi-DC conductivity of warm dense matter measured by single-shot terahertz spectroscopy," Rev. Sci. Instrum. **89**, 10D109 (2018).

[19] S. W. Teitelbaum, B. K. Ofori-Okai, Y.-H. Cheng, J. Zhang, F. Jin, W. Wu, R. D. Averitt, and K. A. Nelson, "Dynamics of a persistent insulator-to-metal transition in strained manganite films," Phys. Rev. Lett. **123**, 267201 (2019).

[20] F. Y. Gao, Z. Zhang, Z. Sun, L. Ye, Y.-H. Cheng, Z. J. Liu, J. G. Checkelsky, E. Baldini, and K. A. Nelson, "Snapshots of a light-induced metastable hidden phase driven by the collapse of charge order," Sci. Adv. **8**, eabp9076 (2022).

[21] P. Plochocka, P. Kossacki, A. Golnik, T. Kazimierczuk, C. Berger, W. A. de Heer, and M. Potemski, "Slowing hot-carrier relaxation in graphene using a magnetic field," Phys. Rev. B **80**, 245415 (2009).

[22] J. Kono, A. H. Chin, A. P. Mitchell, T. Takahashi, and H. Akiyama, "Picosecond time-resolved cyclotron resonance in semiconductors," Appl. Phys. Lett. **75**, 1119–1121 (1999).

[23] G. A. Khodaparast, D. C. Larrabee, J. Kono, D. S. King, S. J. Chung, and M. B. Santos, "Relaxation of quasi-two-dimensional electrons in a quantizing magnetic field probed by time-resolved cyclotron resonance," Phys. Rev. B **67**, 035307 (2003).

[24] G. Dresselhaus, A. Kip, and C. Kittel, "Cyclotron resonance of electrons and holes in silicon and germanium crystals," Phys. Rev. **98**, 368 (1955).

[25] M. Lundstrom, *Fundamentals of Carrier Transport* (Addison-Wesley, Reading, MA, 1990), Vol. 10.

[26] T. Suzuki and R. Shimano, "Time-resolved formation of excitons and electron-hole droplets in Si studied using terahertz spectroscopy," Phys. Rev. Lett. **103**, 057401 (2009).

[27] D. B. But, M. Mittendorff, C. Consejo, F. Teppe, N. N. Mikhailov, S. A. Dvoretskii, C. Faugeras, S. Winnerl, M. Helm, W. Knap *et al.*, "Suppressed Auger scattering and tunable light emission of Landau-quantized massless Kane electrons," Nat. Photonics **13**, 783–787 (2019).

[28] D. Tong, "The quantum Hall effect: TIFR Infosys lectures," arXiv:1606.06687 (2016).